

A Bayesian Approach to Matching Thermonuclear X-ray Burst Observations with Models

A. J. Goodwin^{1,2}, [★] D. K. Galloway^{1,2}, A. Heger^{1,2,3}, A. Cumming⁴, and Z. Johnston^{1,2}

¹*School of Physics & Astronomy, Monash University, Clayton VIC 3800, Australia*

²*also Monash Centre for Astrophysics (MoCA)*

³*Tsung-Dao Lee Institute, Shanghai 200240, China*

⁴*Department of Physics and McGill Space Institute, McGill University, 3550 rue University, Montreal, QC, H3A 2T8, Canada*

Accepted 2019 September 16. Received 2019 September 05; in original form 2019 July 01

ABSTRACT

We present a new method of matching observations of Type I (thermonuclear) X-ray bursts with models, comparing the predictions of a semi-analytic ignition model with X-ray observations of the accretion-powered millisecond pulsar SAX J1808.4–3658 in outburst. We used a Bayesian analysis approach to marginalise over the parameters of interest and determine parameters such as fuel composition, distance/anisotropy factors, neutron star mass and neutron star radius. Our study includes a treatment of the system inclination effects, inferring that the rotation axis of the system is inclined $(69^{+4}_{-2})^\circ$ from the observers line of sight, assuming a flat disc model. This method can be applied to any accreting source that exhibits Type I X-ray bursts. We find a hydrogen mass fraction of $0.57^{+0.13}_{-0.14}$ and CNO metallicity of $0.013^{+0.006}_{-0.004}$ for the accreted fuel is required by the model to match the observed burst energies, for a distance to the source of $3.3^{+0.3}_{-0.2}$ kpc. We infer a neutron star mass of $1.5^{+0.6}_{-0.3} M_\odot$ and radius of $11.8^{+1.3}_{-0.9}$ km for a surface gravity of $1.9^{+0.7}_{-0.4} \times 10^{14}$ cm s⁻² for SAX J1808.4–3658.

Key words: X-rays: bursts – X-rays: binaries – pulsars: individual: SAX J1808.4–3658

1 INTRODUCTION

Accretion-powered millisecond pulsars (AMSPs) are neutron stars with weak ($\sim 10^8$ G) magnetic fields that are accreting matter from a low mass companion star (e.g., Lewin et al. 1993; Chakrabarty & Morgan 1998; Wijnands & van der Klis 1998; Patruno & Watts 2012; Galloway & Keek 2017). These systems are typically transient X-ray sources, and exhibit coherent X-ray pulsations as well as Type I thermonuclear X-ray bursts periodically (e.g., Wijnands 2004). A source goes into outburst when the accretion disc around the neutron star, formed by accretion of matter onto the companion star, reaches a critical state that causes matter to transfer directly onto the neutron star and ignites thermonuclear bursts (e.g., Strohmayer & Bildsten 2006; Galloway & Keek 2017). Type I X-ray bursts are the most frequently observed thermonuclear powered outbursts in nature and provide a unique insight into the nuclear reactions that can occur in extreme environments. They are characterised by a sudden

increase in the X-ray flux of a source in outburst (e.g., Galloway et al. 2008). They can be observed from neutron stars in binary systems, and are thought to be caused by unstable ignition of hydrogen or helium on the surface of an accreting neutron star (e.g., Strohmayer & Bildsten 2006).

The challenge inherent in understanding low-mass neutron star binary systems is estimating system parameters, including the composition of the fuel that drives the thermonuclear burst; and the distance/inclination of the source, which cannot be directly observed as they are kilometre-sized objects at kilo-parsec distances. These parameters are an essential ingredient in modelling and understanding the dense matter of neutron stars and the physical processes behind thermonuclear bursts. Applications range from stellar evolution (with fuel composition of the bursts enabling constraints on the evolution of the companion star and population synthesis) to constraining proton- and carbon-rich nuclear reactions that are difficult to replicate in Earth-bound laboratories.

Neutron stars are the densest directly observable stellar objects known. The study of neutron stars through

[★] E-mail: ajgoodwin.astro@gmail.com

various electromagnetic bands has seen much progress in recent years, furthering the understanding of high-density cold matter and the dense equation of state (e.g. Miller et al. 2019; Degenaar & Suleimanov 2018; Özel & Freire 2016). The recent observation of gravitational waves from merging neutron stars (Abbott et al. 2017) has also seen an increase in efforts to constrain neutron star properties, such as the neutron star mass, radius, spin, and equation of state (e.g., Abbott et al. 2018; Annala et al. 2018; Radice et al. 2018). Constraining these properties is fundamental in the understanding of ultra-dense matter, such as the material that makes up a neutron star, as well as providing additional constraints in the search for more gravitational waves.

Observations of AMSPs that exhibit Type I X-ray bursts are becoming increasingly more accessible, with the Multi-INstrument Burst Archive (MINBAR)¹ providing an extensive collection of processed and analysed X-ray burst data. Observations are limited to the X-ray activity of these sources, providing measurements of the accretion flux, burst flux, and recurrence time of bursts.

Efforts to model burst sources have evolved from early models (e.g., Fujimoto et al. 1987; Taam 1980; van Paradijs et al. 1988) that focused on the correlation between burst energies and recurrence times, to varying success, to more recent models (e.g., Cumming 2003; Galloway et al. 2004; Woosley et al. 2004) which have a heavier focus on the nuclear physics driving the bursts, predicting fuel compositions and accretion rates by implementing more detailed models of the nuclear reaction rates that produce the observed energy generation rates.

These observations and models motivate an effort to combine the data obtained from both, to obtain a deeper understanding of the thermonuclear processes that occur during an X-ray burst, as well as identifying where current models are failing to predict observed properties (e.g., Galloway et al. 2017). The most well-studied transients, such as the accretion-powered millisecond pulsar SAX J1808.4-3658, provide crucial test cases for numerical models of thermonuclear bursts and can be used as standard cases in modelling studies.

Galloway & Cumming (2006) showed that the bursts from SAX J1808.4-3658 were consistent with ignition in an almost pure He environment. The long recurrence times of ≈ 1 day allow enough time for hydrogen to be depleted by thermally-stable hot CNO burning between bursts. By modelling the burst properties, they were able to constrain the hydrogen fraction in the accreted layer, and showed that the observed recurrence times imply a relation between the hydrogen fraction and fraction of CNO elements. As such, SAX J1808.4-3658 provides the best example of pure helium ignited bursts, and validates the theory in which hydrogen depletes before ignition of the X-ray burst in a helium environment.

In this study we develop a new method for matching burst observations with a semi-analytic ignition model, extending the previous work of Galloway & Cumming (2006),

Table 1. Observations of the 2002 October outburst of SAX J1808.4-3658

No.	Burst start time (MJD)	Peak Flux (10^{-9} erg cm $^{-2}$ s $^{-1}$)	Fluence (10^{-6} erg cm $^{-2}$)	α
1	52562.4136	163 \pm 3	2.62 \pm 0.02	–
2	52564.3051	177 \pm 3	2.65 \pm 0.01	107 \pm 2
3	52565.1843	179 \pm 3	2.99 \pm 0.01	118 \pm 2
4	52566.4268	177 \pm 3	3.46 \pm 0.02	128 \pm 2

Notes: The α values are calculated between bursts using Equation 1, assuming 2 bursts occurring between Bursts 1 and 2. Fluxes reported are bolometric fluxes and uncertainties are 1σ confidence levels.

to determine system parameters such as fuel composition, neutron star mass and radius, distance, and inclination. We use a Markov Chain Monte Carlo approach to find the best-fitting system parameters, with uncertainties. In Section 2 we describe the semi-analytic model used in this study, compare it to detailed time-dependent simulations, and describe the MCMC implementation. In Section 3 we report the parameter limits predicted by the model, and describe how well our model matches the observations. Finally, in Section 4, we summarise the results and give our conclusions.

2 METHODS

We used the ignition model of Cumming & Bildsten (2000) (hereafter called SETTLE) to generate burst sequences, which were then compared to Rossi X-ray Timing Explorer (RXTE) Proportional Counter Array (PCA) telescope observations of the 2002 outburst of SAX J1808.4-3658 using a Markov Chain Monte Carlo (MCMC) algorithm. We obtained the ‘best’ model run that matched the observations, providing predictions for parameters such as fuel composition, distance, anisotropies, neutron star mass and radius, that cannot be measured otherwise. We used the python implementation of MCMC, EMCEE (Foreman-Mackey et al. 2013). RXTE observations were obtained from archival data available in MINBAR and shown in Table 1, updated since the initial analysis of this outburst by Galloway & Cumming (2006). Observed properties of the bursts include times, persistent flux, burst fluence and α values. Here, α is defined as the ratio of integrated persistent flux to the fluence, given by

$$\alpha = \frac{F_p c_{\text{bol}} \Delta t}{E_b} \quad (1)$$

where E_b is the burst fluence, Δt is the recurrence time, F_p is the persistent flux, and c_{bol} is the bolometric correction. For c_{bol} we adopted a constant value of 2.12, as in Galloway & Cumming (2006).

In order to determine the accretion rate at the time of a burst, we used persistent flux measurements of the outburst from the PCA and linearly interpolated the values between measurements either side of the burst. This enabled us to obtain a value at the time of each burst, from which an accretion rate was inferred using

$$\dot{m} = c_{\text{bol}} F_p r_1 \quad (2)$$

where F_p is the persistent flux, \dot{m} is the accretion rate, and

¹ <https://burst.sci.monash.edu/minbar/>

r_1 is the scaling factor between the accretion rate and the persistent flux, described in Section 2.3.

2.1 SETTLE

SETTLE is a semi-analytic ignition model developed by Cumming & Bildsten (2000) that integrates the thermal profile of a settling atmosphere to find ignition conditions for a single burst, from which the burst train can be predicted. It applies a one-zone ignition criterion to simple models of the accumulating layer, which allows a survey of parameter space whilst also enabling estimation of the ignition depth. Researchers have applied SETTLE to observations of regular Type I bursters, such as 4U 1820–30 (Cumming 2003), GS 1826–24 (Cumming 2003), and SAX J1808.4–3658 (Galloway & Cumming 2006). The SETTLE model assumes the accumulating fuel layer is heated by hot CNO hydrogen burning within the layer, and a constant flux from deeper layers. It does not include heating from energy released in a previous burst, or the possibility of ignition of unburnt fuel within the ashes of a previous burst (commonly referred to as thermal and compositional inertia; Woosley et al. 2004; see Section 2.2 for corrections we applied to SETTLE to account for some of these simple assumptions). Assuming spherical symmetry, SETTLE does not address complex physics that is currently poorly understood, such as how the burning front spreads across the star after ignition occurs, what determines the number of hotspots on the surface of the star, or the cause of asymmetry near the end of bursts as the material is cooling (e.g., Cavecchi & Spitkovsky 2019).

SETTLE adopts a neutron star mass and radius (e.g., $M_{\text{NS}} = 1.4 M_{\odot}$ and $R_{\text{NS}} = 11.2 \text{ km}$) which then sets the gravitational redshift and surface gravity, where the surface gravity, g , in the X-ray burst layer is given by

$$g = \frac{GM_{\text{NS}}}{R_{\text{NS}}^2} \cdot (1+z) \quad (3)$$

where G is the Gravitational constant, z is the gravitational redshift, M_{NS} is the gravitational neutron star mass and R_{NS} is the neutron star radius in the observer frame.

An X-ray burst is triggered when helium burning becomes unstable at the base of the accumulated layer, at a temperature of $\approx 2 \times 10^8 \text{ K}$ and a density range of $\sim 10^5$ – 10^6 g cm^{-3} . The temperature profile of the accumulating layer of hydrogen and helium is calculated given the accretion rate, and the accumulating layer is allowed to build up until the one-zone condition for a thermal runaway is satisfied at the base of the layer. This condition is met when $d\epsilon_{3\alpha}/dT > d\epsilon_{\text{cool}}/dT$, where $\epsilon_{3\alpha}$ is the energy production rate of helium burning (via the triple alpha reaction) and ϵ_{cool} is the effective local cooling rate. At this point, a thermal instability occurs and the conditions for thermonuclear runaway are met. The temperature profile at ignition is determined such that $d\epsilon_{3\alpha}/dT = d\epsilon_{\text{cool}}/dT$ at the base of the ignition column.

The composition of the ignition column at ignition depends on how much hydrogen has burned before the ignition conditions were met, during the accumulation of the fuel. The amount of hydrogen burned is determined by the local accretion rate, since hydrogen is assumed to burn steadily

at a constant rate via the hot CNO cycle. The rate at which hydrogen burns is thus given by

$$\frac{dY_{\text{H}}}{dt} = \frac{4 \ln 2 Y_{\text{CNO}}}{t_{\frac{1}{2}, \text{CNO}}}, \quad (4)$$

where Y_{CNO} is the parts per nucleon of CNO elements and $t_{\frac{1}{2}, \text{CNO}}$ is the cycle half life, i.e., the sum of the half lives of the isotopes limiting the cycle. In SETTLE, we assume the CNO elements are the β -limited CNO cycle isotopes, ^{14}O and ^{15}O , in their cycle equilibrium abundance values and Y_{CNO} can be computed from

$$Y_{\text{CNO}} = \frac{Z_{\text{CNO}, \beta}}{\bar{A}_{\text{CNO}, \beta}} \quad (5)$$

where $\bar{A}_{\text{CNO}, \beta}$ is the average mass number of the CNO isotopes in the β -limited CNO cycle, given by

$$\bar{A}_{\text{CNO}, \beta} = \frac{t_{\frac{1}{2}, ^{15}\text{O}} A_{^{15}\text{O}} + t_{\frac{1}{2}, ^{14}\text{O}} A_{^{14}\text{O}}}{t_{\frac{1}{2}, ^{15}\text{O}} + t_{\frac{1}{2}, ^{14}\text{O}}}, \quad (6)$$

where A_i is the mass number of species i , $t_{\frac{1}{2}, ^{15}\text{O}} = 122 \text{ s}$ and $t_{\frac{1}{2}, ^{14}\text{O}} = 71 \text{ s}$.

The ratio of the parts per nucleon of ^{14}O to ^{15}O is given by the ratio of their half lives. Thus the mass fractions $Z_{14} = 0.352 Z_{\text{CNO}}$ and $Z_{15} = 0.648 Z_{\text{CNO}}$, giving $\bar{A}_{\text{CNO}, \beta} = 14.653 \text{ g mol}^{-1}$.

The energy production rate of hydrogen burning via the CNO cycle, ϵ_{H} , is given by

$$\epsilon_{\text{H}} = \frac{d}{dt} Y_{\text{H}} E_{\text{H}},$$

where E_{H} is the energy produced from burning $4 \text{ } ^1\text{H}$ to ^4He . E_{H} is given by the change in mass excess less the energy carried away by neutrinos, $E_{\text{H}} = 6.03 \times 10^{18} \text{ erg g}^{-1}$. Thus, ϵ_{H} is given by

$$\epsilon_{\text{H}} = 5.94 \times 10^{13} \frac{Z_{\text{CNO}, \beta}}{0.01} \text{ erg g}^{-1} \text{ s}^{-1}, \quad (7)$$

where $Z_{\text{CNO}, \beta}$ is the mass fraction of CNO nuclei in the β -limited CNO cycle, computed as outlined above.

We also compare to the Sun as a reference point with its own, different, distribution of the CNO isotopes, with $\bar{A}_{\text{CNO}, \odot} = 14.688$, such that a given CNO metallicity translates into a slightly different value of Y_{CNO} . Using the solar abundance ratios for CNO isotopes from Lodders et al. (2009), one obtains:

$$\epsilon_{\text{H}} = 5.93 \times 10^{13} \frac{Z_{\text{CNO}, \text{scaled } \odot}}{0.01} \text{ erg g}^{-1} \text{ s}^{-1} \quad (8)$$

which is remarkably similar to the value using the β -limited Z value reference, though only by coincidence, not by design.

Throughout the remainder of this paper all values of metallicity refer exclusively to the β -limited CNO metallicity, which is the relevant value for SETTLE. The reference value of 0.01 used here is indeed very close to the solar mass fraction of CNO isotopes given by Lodders et al. (2009) as 0.01001.

Summarising, the time to burn all of the hydrogen (t_{H})

is dependent only on the metallicity and initial hydrogen abundance. The time to burn hydrogen is thus

$$t_{\text{H}} = \frac{Y_{\text{H}}}{Y_{\text{CNO}}} \frac{t_{\frac{1}{2},^{15}\text{O}} + t_{\frac{1}{2},^{14}\text{O}}}{4 \ln 2} = 20.45 \left(\frac{X_0}{0.7} \right) \left(\frac{0.01}{Z_{\text{CNO}}} \right) \text{h} \quad (9)$$

where X_0 is the initial hydrogen mass fraction of the accreted fuel. This sets the minimum recurrence time required for pure helium bursts. Note that we have updated this equation from the original work of [Cumming & Bildsten \(2000\)](#), and it is the time to burn hydrogen locally on the neutron star surface, for the observer this timescale is longer by a redshift factor $1+z$. For higher accretion rates ($\dot{m} \gtrsim 0.04 \dot{m}_{\text{Edd}}$ ²) helium burning becomes unstable before sufficient time has passed for all of the hydrogen to be burned, resulting in ignition occurring in a hydrogen rich environment. For lower ($\dot{m} \lesssim 0.04 \dot{m}_{\text{Edd}}$) accretion rates, there is sufficient time for all of the hydrogen to be burned before ignition, allowing a pure helium layer to accumulate before ignition, and a helium rich environment for the burst.

The column depth at which hydrogen runs out (y_{d}) is given by:

$$y_{\text{d}} = 6.9 \times 10^8 \left(\frac{\dot{m}}{0.01 \dot{m}_{\text{Edd}}} \right) \left(\frac{0.01}{Z_{\text{CNO}}} \right) \left(\frac{X_0}{0.7} \right) \text{g cm}^{-2} \quad (10)$$

If helium ignites at a column depth $y < y_{\text{d}}$, a mixed H/He burst occurs; and if helium ignites at a column depth $y > y_{\text{d}}$, a pure helium layer has time to accumulate and ignition occurs in a pure helium environment.

Once ignition conditions are met, the burst parameters are calculated based on the total mass in the ignition column and its composition. The burst energy is calculated by assuming complete burning of the H/He layer, and the accreted material is assumed to cover the whole surface of the neutron star. The thickness of the accumulated layer at ignition determines the recurrence time of the bursts.

2.1.1 Updates to SETTLE

When hydrogen remains at the time of ignition, and bursts ignite in a mixed H/He environment, there is extra energy released by the triple-alpha process due to proton capture by ^{12}C . To avoid a discontinuity in accretion rate–recurrence time parameter space at the transition zone between mixed H/He bursts and pure He bursts, we gradually switched on the factor that multiplies the triple alpha reaction energy generation rate to account for the $^{12}\text{C}(p,\gamma)$ reaction when protons begin running out at the critical H fraction of $X = 1/7$ (since the ratio of protons to alpha particles is 2 : 3). The gradual switch on of this multiplicative factor was not a feature of [Cumming & Bildsten \(2000\)](#)'s original code.

We updated some of the energy and rate values used in SETTLE. We corrected the energy generation of hydrogen burning via the CNO cycle such that $\epsilon_{\text{H}} = 5.94 \times 10^{15} \text{erg g}^{-1} \text{s}^{-1}$ (used to be $5.8 \times 10^{15} \text{erg g}^{-1} \text{s}^{-1}$). We also used an updated version for the total nuclear energy released per unit mass in an X-ray burst as calibrated by

² \dot{m}_{Edd} is the Eddington accretion rate, given by $\dot{m}_{\text{Edd}} = 1.75 \frac{0.7}{1+X} \times 10^{-8} M_{\odot} \text{yr}^{-1}$, where X is the H mass fraction

[Goodwin et al. \(2018\)](#) using KEPLER models, $Q_{\text{nuc}} = 1.35 + 6.05 \bar{X} \text{MeV/nucleon}$, where \bar{X} is the average hydrogen mass fraction of the ignition column. The ignition depth correction we applied due to differences between SETTLE and KEPLER is described in Section 2.2

Using KEPLER models with fully time-dependent accretion rates, [Johnston et al. \(2018\)](#) found that using constant accretion rates (averaged between bursts) can systematically underestimate the burst recurrence times when the slope of the accretion rate is negative (see Figure 4 of that paper). Because SETTLE implicitly uses averaged accretion rates, we accounted for this effect by multiplying each predicted recurrence time by a correction factor, as determined by the linear approximation from [Johnston et al. \(2018\)](#). These correction factors ranged from approximately 0.9–1.0 for our modelled bursts. The correction factors we adopted are specific to SAX J1808.4–3658 and will either need to be recalculated or made more generally applicable if this method is applied to a different system. To rigorously test the influence of these correction factors we ran the code without the scaling factors and found that while the central value of the distance, hydrogen fraction, metallicity, and base flux shifted, the parameters still agreed within 1- σ uncertainty of the model run with the scaling factors.

2.2 Code Verification

A simple code such as SETTLE can be run in seconds, enabling multiple instances of the code to be run, and a marginalising method such as MCMC possible. Other codes, such as KEPLER ([Woosley et al. 2004](#)), use bigger nuclear reaction networks and a more complex treatment of the neutron star atmosphere during outburst, at the cost of computational expense and runtime. KEPLER solves the full time-dependent stellar structure equations, following the evolution of temperature and composition at each depth in the neutron star envelope over many cycles of bursts. To assess the limitations of SETTLE, we ran a comparison with some KEPLER models, and implemented corrections to SETTLE to account for some of the differences we found. [Woosley et al. \(2004\)](#) provided a limited comparison between some SETTLE and KEPLER models, and found that, in general, the agreement was good, although with SETTLE consistently overestimating the burst energies and recurrence times. The authors attribute the discrepancy between the SETTLE and KEPLER models to the lack of compositional inertia in the SETTLE models.

We compared the predicted fluences (E_{b}) and recurrence times (Δt) of the two codes for a range of hydrogen mass fractions (X), CNO mass fractions (Z), accretion rates (\dot{m}) and base fluxes (Q_{b}). In order to allow meaningful comparison, we redshifted the KEPLER recurrence times by multiplying by $1+z$, as KEPLER calculates recurrence time in the reference frame of the neutron star, whereas SETTLE calculates recurrence time in the reference frame of a distant observer. In both codes we fixed $M_{\text{NS}} = 1.4 M_{\odot}$ and $R_{\text{NS}} = 11.2 \text{km}$. We also increased the SETTLE Q_{b} value by 0.1 MeV/nucleon when comparing to KEPLER to account for thermal inertia ([Cumming & Bildsten 2000](#)).

On initial comparison we found the SETTLE recurrence times and fluences were at least $\sim 30\%$ higher than the KE-

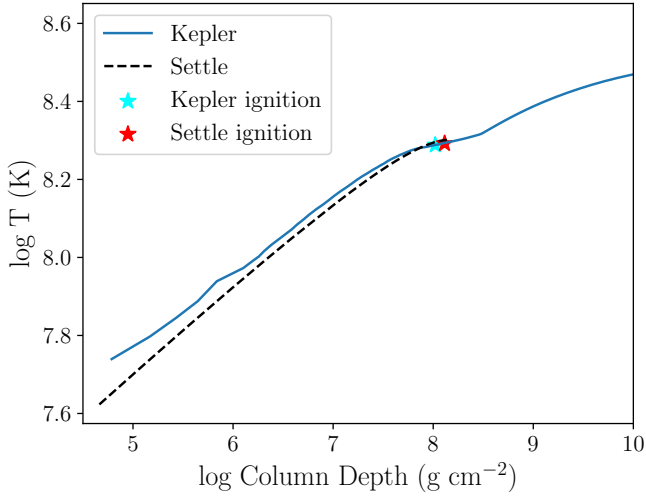


Figure 1. Comparison of the temperature profile of SETTLE (black dashed) and KEPLER (blue solid) models at the ignition of a burst. Stars indicate the ignition depth of the burst for each model. Model conditions: $X = 0.2$, $z = 0.02$, $\dot{m} = 0.2 \dot{m}_{\text{Edd}}$, $Q_b = 0.1$ Mev/nucleon.

PLER predictions. We compared the temperature profiles of the ignition column for each code, shown in Figure 1.

We found the temperature profile of SETTLE was overall cooler than KEPLER, causing a longer recurrence time, deeper ignition, and thus brighter bursts. Since KEPLER provides a more complex analysis of the underlying physics, we decided to correct the ignition depth of SETTLE such that it matched the KEPLER ignition depth. To do this we multiplied the SETTLE ignition depth by a factor of 0.65. Reducing the ignition depth reduced the recurrence time and fluences of the SETTLE bursts and produced the comparison shown in Figure 2.

In Figure 2 for higher hydrogen fractions ($X = 0.6$ and 0.7) there is a significant difference between the predicted fluences and recurrence times of the SETTLE and KEPLER bursts across all accretion rates. There is much better agreement at lower hydrogen fractions ($X < 0.5$) and lower accretion rates ($\dot{m} < 0.1 \dot{m}_{\text{Edd}}$ between the two codes. For the purpose of this paper we note that for the source we are investigating, SAX J1808.4–3658, observations indicate that it has a slightly depleted hydrogen fraction and low ($\approx 4\%$ Eddington) accretion rate, so it is within the parameter space that SETTLE agrees well with KEPLER.

Fundamental differences between the two models can be attributed primarily to the fact that SETTLE has a one-zone ignition criterion which uses a local approximation for the cooling, whereas KEPLER follows the detailed cooling as a function of depth. Other differences could arise due to the fact that SETTLE assumes there is no triple-alpha burning during the accumulation of fuel, SETTLE assumes that all of the accreted fuel is burnt in a single burst, and the burst train is generated without accounting for subsequent bursts occurring in the ashes of previous bursts. Finally, SETTLES uses an approximate formula for the nuclear energy generation of the bursts, that has been calibrated to KEPLER predictions, but still is not the same as calculating the full nuclear reaction network, with thermal inertia included. As

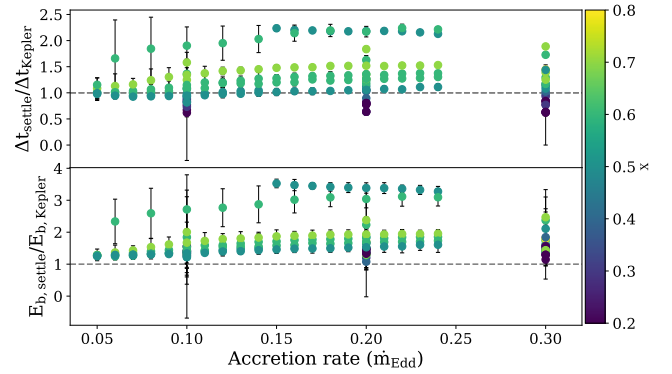


Figure 2. Comparison of the predicted recurrence times (top) and burst fluences (bottom) for the SETTLE and KEPLER models for a range of accretion rates (\dot{m} , expressed as a fraction of \dot{m}_{Edd}), after the ignition depth in SETTLE has been reduced by 45%. The dashed line shows the one-one relation between the two predictions. Some of the models have different CNO metallicities and base heating, causing some variances in the predictions for the same accretion rate and hydrogen mass fraction.

a caveat we note that calibrating to KEPLER introduces a different kind of model bias. Since there have been no comprehensive studies done between KEPLER and other similar codes, we do not understand how accurately KEPLER models the true physics of these systems.

2.3 MCMC

We used a Python implementation of MCMC (EMCEE; Foreman-Mackey et al. 2013) to estimate posterior distributions of the properties predicted by SETTLE, based on the known values of the observed properties of the burst train (time, E_b and α). We defined a likelihood function, given by Equation 11, and prior ranges for each parameter. We used a simple Gaussian likelihood function where the variance was underestimated by some fractional amount, f , and the overall likelihood is the sum of the individual likelihoods for each parameter i ,

$$L(x_i|\theta, \text{model}) = \frac{1}{\sigma_i f_i \sqrt{2\pi}} \exp \left[\frac{-(x_i - \text{model})^2}{2f_i \sigma_i} \right] \quad (11)$$

where σ_i is the observed uncertainty, x_i is the observed parameter value (time, fluence, and alpha), model is the parameter value predicted by the model, and θ are our parameters of interest. The parameters of interest we defined are hydrogen mass fraction X , metallicity Z , which is defined as the mass fraction of CNO elements (all in ^{14}O and ^{15}O), base flux Q_b , neutron star mass M , neutron star radius R and three scaling factors, r_1 , r_2 , and r_3 .

The 3 scaling factors, r_1 , r_2 , and r_3 are defined as in Galloway & Cumming (2006), given in Equations 12, 13, and 14,

$$r_1 = \frac{\dot{m}_i}{c_{\text{bol}} F_{p,i} \xi_p} \quad (12)$$

where \dot{m}_i is the accretion rate between burst $i - 1$ and burst i , ξ_p is the persistent anisotropy (defined in Section

3.1, $F_{p,i}$ is the mean 2–25 keV persistent flux between burst $i - 1$ and i (in units of $10^{-9} \text{ erg cm}^{-2} \text{ s}^{-1}$, from interpolation) and c_{bol} is the bolometric flux correction.

$$r_2 = \frac{\alpha}{\alpha_{\text{pred}}} \quad (13)$$

where α is the observed value (Equation 1) and $\alpha_{\text{pred}} = 290/Q_{\text{nuc,pred}}$.

$$r_3 = \frac{E_{\text{b}}/10^{-9}}{L_{\text{b,pred}} \xi_{\text{b}}} \quad (14)$$

where $L_{\text{b,pred}}$ is the predicted burst luminosity in units of $10^{39} \text{ erg s}^{-1}$ and E_{b} is the observed burst fluence.

We initialised the parameters in a tiny ($\sim 10^{-3}$) Gaussian ball around the initial value. We ran the MCMC chains with 300 walkers for 2,000 steps, and discarded the first 200 steps in each chain to account for burn-in. See Section 3.4 for information on the tests we ran to ensure the MCMC chains were fully converged and independent of initial walker positions.

2.4 Priors

For each parameter except metallicity, mass and radius, we used a uniform prior, where we chose an acceptable range based on observations or theoretical assumptions. For metallicity (Z_{CNO}) we chose a more informed prior, using a synthetic survey of the Milky Way in the location of SAX J1808.4-3658 at 2–4 kpc generated by the Galaxia code (Sharma et al. 2011) to determine a likely distribution of the metallicity, given by Equation 15 and shown in Figure 3.

$$[\text{Fe}/\text{H}] \sim \phi\left(3 + \frac{3}{4}\right) - 3 \quad (15)$$

where $\phi \sim \mathcal{B}(10, 3)$ is a Beta distribution with $\alpha = 10$ and $\beta = 3$, and the linear translation limits the metallicity prior to have support between $[\text{Fe}/\text{H}] = -3$ and $+0.75$ (i.e., $0.00001 < Z_{\text{CNO}} < 0.056$).

For mass and radius we also imposed a more informed prior based on the models of Steiner et al. (2018), who used observations of eight quiescent low mass X-ray binaries in globular clusters to determine the neutron star mass–radius curve and the equation of state. Steiner et al. (2018) used a fixed mass grid and varied radius according to their chosen equation of state and observations of radii. We chose the simplest of their models (‘baseline’) and used the probability distribution given in Figure 2.4 for the relationship between mass and radius. We also constrained mass and radius to: $1.15 M_{\odot} < M < 2.5 M_{\odot}$ and $9 \text{ km} < R < 17 \text{ km}$. This prior effectively checks if the masses and radii predicted by the model are consistent with the expected mass–radius relation of low mass X-ray binaries in globular clusters. It provides a probability of the predicted radius given the predicted mass.

3 RESULTS

We report the posterior limits for the predicted system parameters in Table 2, reporting the mean value and the 68th

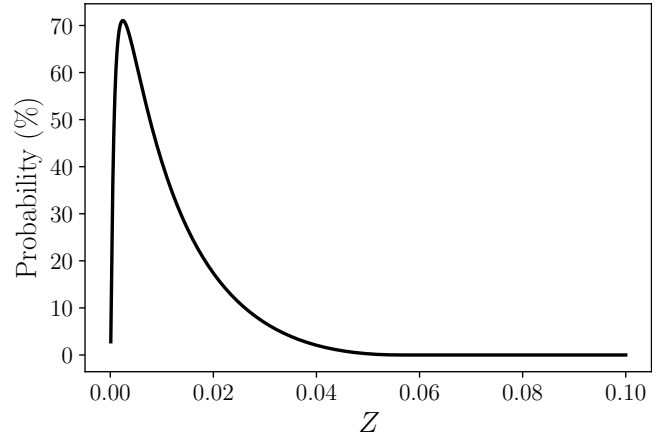


Figure 3. The probability distribution assumed for metallicity (Z), based on a simple model of the Galaxy in the location of SAX J1808.4-3658 at 2–4 kpc.

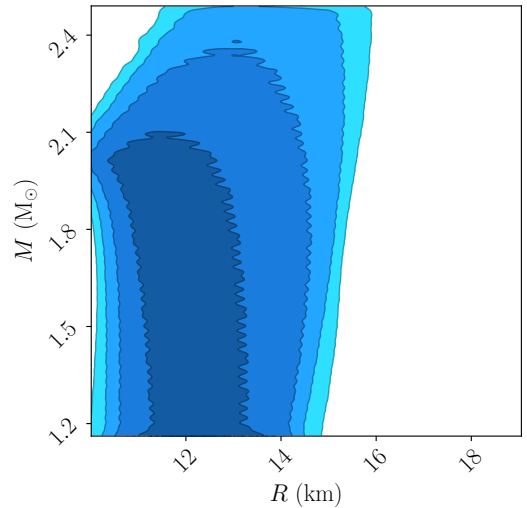


Figure 4. Steiner et al. (2018) probability distribution for NS radius as a function of mass based on observations of low mass X-ray binaries in globular clusters. Contour levels shown are 1σ intervals up to 5σ .

percentile limits of the distributions for the uncertainties. Additional model runs are shown in the Appendix, including one that replicates Galloway & Cumming (2006) with fixed mass and radius and one with a uniform prior in mass and radius.

The times and fluences of the 6 predicted bursts are plotted in Figure 5, as well as the 4 observed bursts. We predict 3 bursts that were not observed, but that cannot be ruled out by observations, since they occur during periods that the telescope was not observing. The two bursts predicted between the first and second observed bursts were also predicted by Galloway & Cumming (2006) and Johnston et al. (2018). The predicted burst properties agree reasonably well with the predictions from Johnston et al. (2018), who used KEPLER to model this outburst without doing an exhaustive parameter space exploration such as we have done in this work. Interestingly, Johnston et al. (2018) also

Table 2. SAX J1808.4-3658 derived neutron star parameters

Parameter	Value	Units
X	$0.58^{+0.13}_{-0.14}$	
Z	$0.013^{+0.006}_{-0.004}$	
Q_b	$0.4^{+0.3}_{-0.2}$	MeV/nucleon
M	$1.5^{+0.6}_{-0.3}$	M_\odot
R	$11.8^{+1.3}_{-1.0}$	km
\dot{m}_{\max}	$0.037^{+0.002}_{-0.002}$	\dot{m}_{Edd}
g	$1.9^{+0.7}_{-0.4}$	$10^{14} \text{ cm s}^{-2}$
$1+z$	$1.27^{+0.13}_{-0.05}$	
d	$3.3^{+0.3}_{-0.2}$	kpc
ξ_b	$0.74^{+0.10}_{-0.10}$	
ξ_p	$0.87^{+0.12}_{-0.10}$	
$\cos i$	$0.36^{+0.07}_{-0.04}$	

Notes: g and $1+z$ are calculated based on the M and R values, using Equation 3. \dot{m}_{\max} is the maximum inferred accretion rate using Equation 2.

Table 3. SAX J1808.4-3658 predicted burst parameters

Burst	\bar{X}	α	Δt (hours)
2	$0.20^{+0.06}_{-0.06}$	108^{+12}_{-9}	14.7
3	$0.20^{+0.06}_{-0.06}$	107^{+12}_{-9}	14.4
4*	$0.19^{+0.05}_{-0.06}$	110^{+11}_{-9}	16.1
5*	$0.16^{+0.04}_{-0.04}$	117^{+10}_{-9}	19.4
6*	$0.12^{+0.03}_{-0.03}$	126^{+9}_{-7}	31.2
7	$0.07^{+0.02}_{-0.02}$	139^{+6}_{-5}	56

Notes: "*" indicates this burst was observed by *RXTE*. Burst 1 is excluded as it was used as a reference burst and we did not infer properties for this burst. \bar{X} is the average hydrogen mass fraction of the ignition column.

predict a very bright burst at late time, ≈ 7 days after the first observed burst.

Burst properties for individual bursts inferred by the model are listed in Table 3. The recurrence time for each burst is predicted to fall in the range 14 – 56 hours. The time to exhaust hydrogen and ignite bursts in a pure helium environment is 13.0 hours at this accreted fuel composition (Equation 9). These predicted recurrence times and their respective accretion rates indicate that sufficient time passes between each burst for the accreted hydrogen to be completely burned by the hot CNO cycle, and we have ignition occurring in a pure helium environment, as has been previously concluded by Galloway & Cumming (2006); Johnston et al. (2018). The low \bar{X} values for each burst confirms this, with $\bar{X} < 0.2$ for all bursts.

The probability contours and posterior distributions for X , Z , Q_b , d , ξ_b , and ξ_p are plotted in Figure 6. There is a positive correlation between X and Z , which was also found by Galloway & Cumming (2006). This correlation is due to the relationship between recurrence time and fuel composi-

tion, since provided all of the H is exhausted before ignition, there are multiple combinations of X and Z that reproduce the observed recurrence time.

3.1 Distance and Anisotropies

We used the scaling parameters r_1 , r_2 , and r_3 to obtain posterior distributions for the distance and emission anisotropies of the source, and thus the inclination, shown in Figure 6. Relating the scaling parameters to their corresponding physical parameters gives:

$$r_2 = 0.74816 \left(\frac{M_{\text{NS}}}{1.4 M_\odot} \right) \left(\frac{R_{\text{NS}}}{11.2 \text{ km}} \right)^{-1} \left(\frac{Q_{\text{nuc}}}{Q_{\text{nuc,pred}}} \right)^{-1} \left(\frac{\xi_p}{\xi_b} \right) \quad (16)$$

$$r_3 = 63.23 \left(\frac{d}{10 \text{ kpc}} \right)^{-2} \left(\frac{R_{\text{NS}}}{11.2 \text{ km}} \right)^2 \left(\frac{1+z}{1.258} \right)^{-1} \left(\frac{Q_{\text{nuc}}}{Q_{\text{nuc,pred}}} \right) \xi_b \quad (17)$$

Assuming $Q_{\text{nuc}} = Q_{\text{nuc,pred}}$, this gives the following set of equations which enable calculation of d , ξ_b and ξ_p using the three scaling factors.

$$\xi_p = r_1 \left(\frac{10}{d} \right)^2 \quad (18)$$

$$\xi_b = \frac{r_2 \xi_p}{0.74816} \quad (19)$$

$$d = 10 \sqrt{\frac{63.23 \xi_b}{r_3}} \text{ kpc} \quad (20)$$

Using these equations, we obtained posteriors on distance (d), burst anisotropy (ξ_b) and persistent anisotropy (ξ_p), shown in Figure 6 and values reported in Table 2. He & Keek (2016) modelled the relationship between anisotropy factors and inclination in low mass binaries with different disc shapes. They considered 4 different disc geometries, motivated by an effort to match observations of high reflection fractions observed in a couple of superbursts. Since SAX J1808.4-3658 has never shown evidence of such high reflection fractions, we chose the simplest disc geometry described by He & Keek (2016), Model A, corresponding to a flat disc. He & Keek (2016) Model A is approximated by Equation 21, which we used to also obtain a posterior distribution for $\cos i$, based on the inferred anisotropy factors.

$$\frac{\xi_p}{\xi_b} = \frac{0.5 + |\cos i|}{2|\cos i|} \quad (21)$$

where i is the inclination of the system, the angle between the rotation axis and the direction from which the system is viewed by an observer.

For this disc Model A, we infer a distance to SAX J1808.4-3658 of $3.3^{+0.3}_{-0.2}$ kpc, which agrees within uncertainty of the predictions of Galloway & Cumming (2006) of 3.1–3.8 kpc. We note that Galloway & Cumming (2006) did not account for the anisotropy of emission when inferring their distance estimate. Applying our predicted anisotropy factors to their distance estimate reduces their estimate to 2.7–3 kpc, still within our predicted distance range.

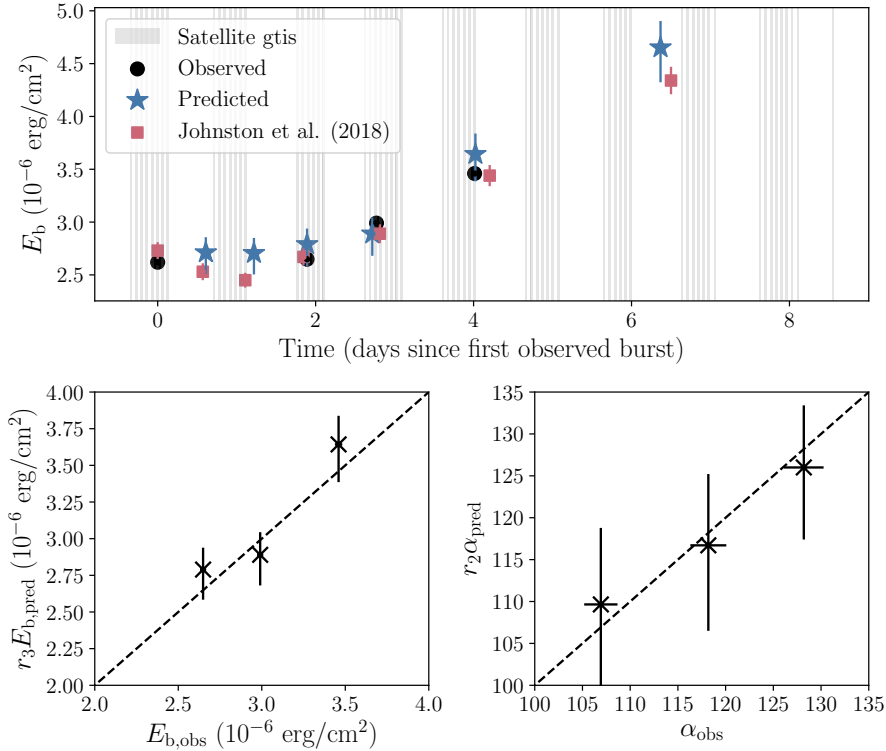


Figure 5. Top: predicted burst times and fluences (blue stars), observed bursts times and fluences (black circles) and predicted burst times and fluences from [Johnston et al. \(2018\)](#) (red squares). The grey regions show the satellite observing periods (‘good time intervals’). Bottom left: r_3 times the predicted burst fluences vs observed burst fluences. Dashed line is the one-to-one relation. Bottom right: r_2 times the predicted alphas vs observed alphas. Dashed line is the one-to-one relation.

3.2 Neutron Star Mass and Radius

We infer a neutron star mass of $M_{\text{NS}} = 1.5^{+0.6}_{-0.3} M_{\odot}$ based on the gravity and gravitational redshift required by the model that gives the best match to the observations. Since the neutron star in this system has been accreting matter periodically, we expect it to be more massive than a single non-binary neutron star (e.g. [Kiziltan et al. 2013](#)). Canonically, the neutron star mass is assumed to be $M_{\text{NS}} = 1.4 M_{\odot}$, and recent works constraining NS mass and radii have found the NS mass could be between 1.1 – $2.2 M_{\odot}$ (e.g., [Antoniadis et al. 2016](#)). There has been extensive work in trying to estimate the mass of SAX J1808.4–3658 with no consensus on the value, but the general finding that it is more massive than the canonical value of $1.4 M_{\odot}$ (e.g. [Heinke et al. 2009](#); [Elebert et al. 2009](#); [Morsink & Leahy 2011](#)). If the NS mass is larger than the usually assumed NS mass, this could indicate that some of the accreted matter is not burned in the observed X-ray bursts, as was modelled by [Goodwin et al. \(2018\)](#), however, due to the uncertainty of our mass prediction this result is not significant.

The posterior distributions and probability contours for mass and radius are plotted in Figure 7, coloured by surface gravity. The prior we used for mass and radius is plotted in red.

From Figure 7 it appears that there is a preferred surface gravity loosely driving the correlation between mass and radius, with the preferred surface gravity being 1.9×10^{14} g cm $^{-2}$. Interestingly, the radius posterior peaks at

a radius lower than the peak radius of the prior distribution, indicating that the model fit prefers a smaller radius. The model is thus sensitive to changes in radius. We explore this further in Section 4, in which we compare model runs with fixed mass and radius and flat mass and radius priors.

3.3 Binary System Parameters and Inclination

The mass function of the binary orbit is given by

$$f_x = \frac{(M_c \sin i)^3}{(M_{\text{NS}} + M_c)^2} = \frac{4\pi^2 (a_x \sin i)^3}{GP_{\text{orb}}^2} \quad (22)$$

where i is the binary inclination, M_c is the companion star mass and M_{NS} is the neutron star mass (e.g., [Chakrabarty & Morgan 1998](#); [Bildsten & Chakrabarty 2001](#)).

Setting the projected semi-major axis, $a_x \sin i = 62.809$ light – ms ([Chakrabarty & Morgan 1998](#)) and orbital period, $P_{\text{orb}} = 2.01$ h gives $f_x = 3.8 \times 10^{-5} M_{\odot}$. This leaves M_{NS} , i , and M_c . Our MCMC algorithm uses SETTLE to find $M_{\text{NS}} = 1.5^{+0.6}_{-0.3} M_{\odot}$. Given estimates of $M_c = 0.02 - 0.011 M_{\odot}$ (e.g., [Bildsten & Chakrabarty 2001](#)) and using Equation 22, the mass function gives $\cos i = 0.62^{+0.09}_{-0.08}$ ($i = (64^{+37}_{-20})^{\circ}$).

Lack of deep X-ray eclipse rules out $i > 82^{\circ}$ ($\cos i < 0.15$) ([Chakrabarty & Morgan 1998](#)). There is a 2% modulation in X-ray intensity at the orbital period, which suggests that

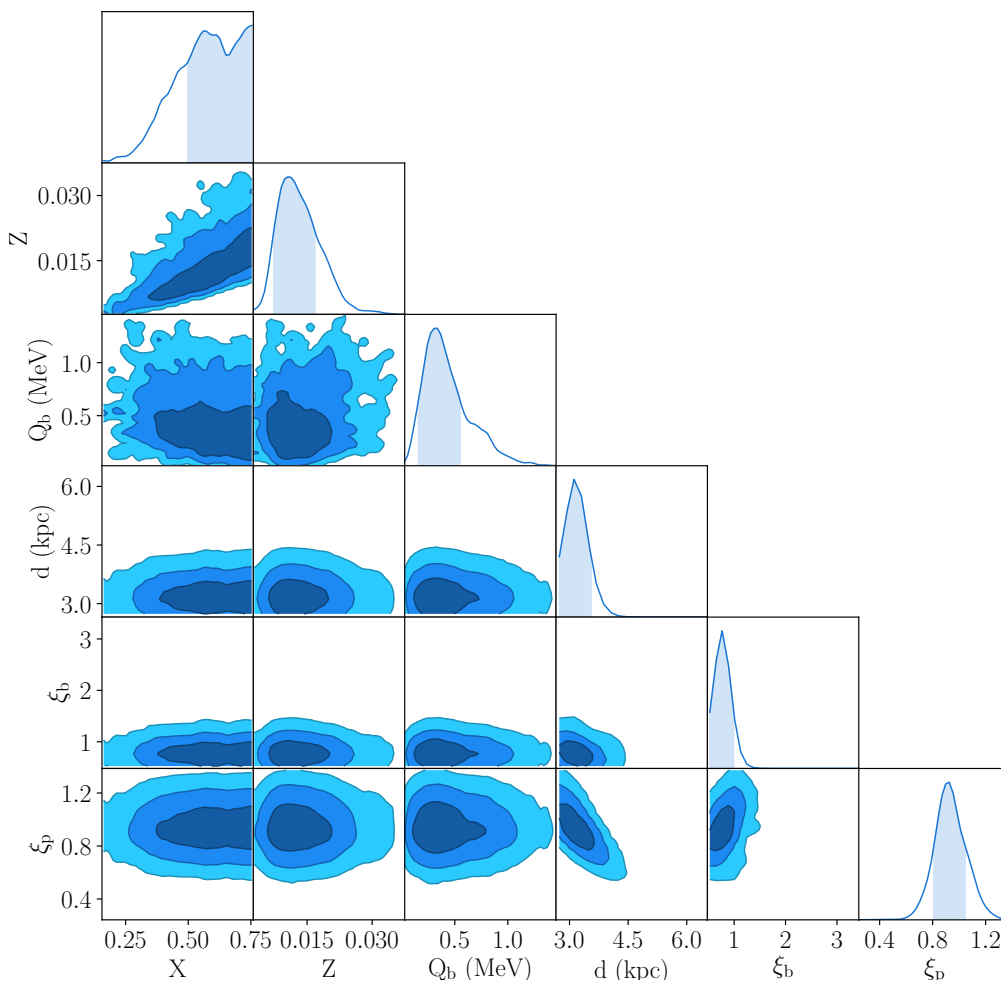


Figure 6. 2-dimensional projection of the posterior probabilities of hydrogen mass fraction (X), metallicity (Z), base heating rate (Q_b), distance (d) and anisotropy factors (ξ_b and ξ_p) of SAX J1808.4–3658. Histograms along the diagonal show the marginalised probabilities of the individual parameters. Contour levels are the 1, 2, and 3 σ bounds.

i must be large enough to allow partial X-ray blockage from some circumbinary material (Bildsten & Chakrabarty 2001). Those authors rule out face on inclination due to the 2 hour single-peaked modulation in the optical intensity, confirmed by Homer et al. (2001). The flux minimum occurs when the neutron star is behind the companion, implying that the X-ray heating of the companion is the origin of the modulation, which would have no effect in a face on system. Our best estimate gives $\cos i = 0.36^{+0.07}_{-0.04}$ ($i = (69^{+4}_{-2})^\circ$), which agrees within 3σ of $\cos i = 0.62^{+0.09}_{-0.08}$ found using the mass function, and is within the ranges predicted by Bildsten & Chakrabarty (2001) and Wang et al. (2001). More recently, Wang et al. (2013) and Cackett et al. (2009) have attempted to constrain the inclination through optical modelling and iron line modelling respectively. Wang et al. (2013) found $i = (50^{+6}_{-5})^\circ$ and Cackett et al. (2009) found $i = (55^{+8}_{-4})^\circ$ (1σ uncertainties). The Cackett et al. (2009) estimate agrees within 2σ of our best estimate, and the Wang et al. (2013) estimate agrees within 3σ .

Since the anisotropy factors are determined independently in this method, we checked the self consistency of

these factors with the relationships predicted by the Fujimoto (1988) and He & Keek (2016) models in Figure 8.

SAX J1808.4–3658 is in the hard spectral state during its outbursts and due to its nature as an accreting pulsar, it is predicted to have a truncated disc (e.g., Psaltis & Chakrabarty 1999). The Fujimoto et al. (1981) and He & Keek (2016) models do not model for a truncated disc, and thus we do not expect any of them to match our predictions perfectly. We could not decisively conclude which of the models matched our predictions best, as they all pass through the 1σ confidence area in Figure 8, motivating us to use the simplest model, He & Keek (2016) Model A.

3.3.1 Wind loss

Recent research has found that a significant amount ($\approx 30\%$) of the nuclear energy of a Type I X-ray burst could be used to unbind matter from the neutron star surface, ejected in a wind. Yu & Weinberg (2018) found that wind losses can cause up to 30% loss of nuclear energy in ejecting material from the system. We do not correct for wind loss in our models as upon testing it simply reduced the predicted distance

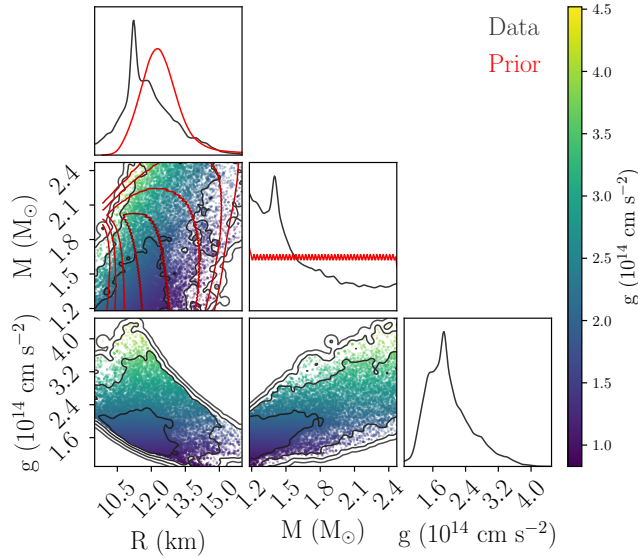


Figure 7. 2-dimensional projection of the posterior probabilities of NS mass (M), NS radius (R) and surface gravity (g) of SAX J1808.4-3658 (black and coloured by g) and the NS mass and radius prior probability distribution from Steiner et al. (2018) (red). Histograms along the diagonal show the marginalised probabilities of the individual parameters and contour levels are 1σ intervals up to 5σ .

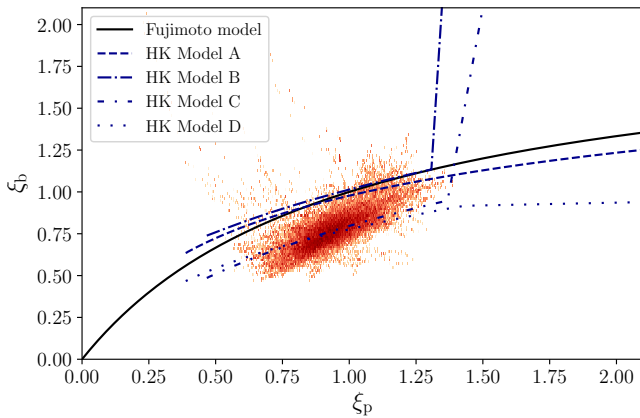


Figure 8. The distribution of the 1σ MCMC predictions for the anisotropy factors, ξ_p and ξ_b (orange) and the relationship between ξ_p and ξ_b as predicted by the He & Keek (2016) (HK) and Fujimoto (1988) models for different disc shapes.

by $\approx 7\%$, with mass loss causing the source to be predicted closer due to fainter bursts being predicted.

3.4 Chain Convergence and MCMC performance

The convergence of MCMC chains is notoriously difficult to assess. Goodman & Weare (2010) recommend using the integrated autocorrelation time (τ) to quantify the effects of sampling error on the results. The autocorrelation time provides a measure of the large time error of the Monte Carlo estimator, and so is a reliable indicator of the accuracy of the sampler by measuring the asymptotic variance in the

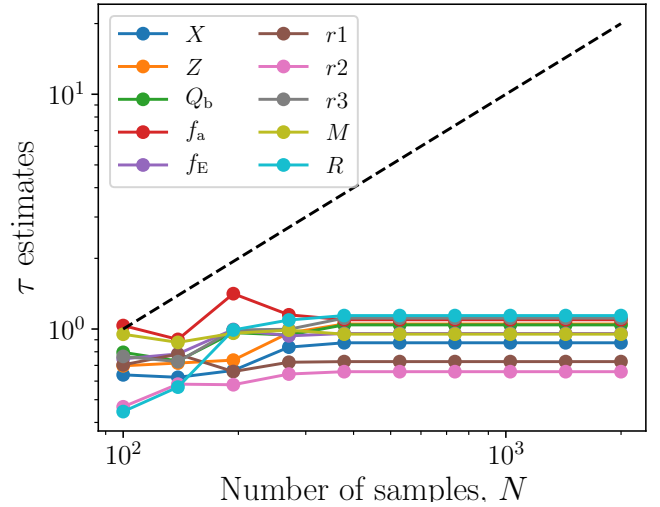


Figure 9. The evolution of the autocorrelation time (τ) with the number of samples taken for the 10 parameters varied with MCMC. The black dashed line is the $\tau = N/100$ line.

limit of long chains. This essentially measures the effective number of independent samples, and enables estimation of the number of samples required to reduce the relative error on the target integral to a few percent. Foreman-Mackey et al. (2013) recommend running the chains for at least 50τ samples (or conservatively 100τ samples).

In Figure 9 the autocorrelation time of each parameter we varied is plotted as a function of the number of samples. The autocorrelation time is not reliably estimated early on, as there are not enough samples. As more samples are taken, the autocorrelation time estimate becomes more accurate, and after ≈ 500 samples, the autocorrelation time converged on a single value for all of the parameters. By 2,000 samples, all of the autocorrelation estimates are well below the $\tau = N/100$ line, indicating this is an accurate estimate of the autocorrelation time. The largest autocorrelation time is <10 so the chains should be converged according to this convergence test after 1,000 steps. We ran the chains for 2,000 steps and 300 walkers to ensure they would be fully converged.

The acceptance fraction of the samples is a widely used measure to check the performance of MCMC. The acceptance fraction is the number of proposed steps that are accepted, and will be small if too many steps are rejected and large if too many steps are accepted (Foreman-Mackey et al. 2013). The general consensus is that the acceptance fraction should be between 0.2–0.5 (e.g., Gelman et al. 1996), however, it depends on the model and situation. The acceptance fraction of our final run was 0.14, which is lower than 0.2 but not unreasonably low. As a test, we ran the MCMC code returning only the prior (excluding the likelihood and thus model call) and found an acceptance fraction of 0.11. We can thus conclude that the prior limits are constraining parameter space and causing a larger than usual amount of steps to be proposed outside the allowed domain and be rejected.

A final test we ran to ensure the end walker positions were independent of the initial positions was to change the size of the Gaussian ball the walkers were initialised around

by a factor of 100. This did not affect the marginalised posterior distributions of each parameter.

4 DISCUSSION AND CONCLUSIONS

We have used a Bayesian approach to successfully match observed burst fluence, alpha, and recurrence times with the SETTLE model to infer system parameters of an accreting millisecond pulsar in outburst. The properties of the bursts observed from SAX J1808.4–3658 indicate they arrive in helium rich fuel, given the relatively short length, low flux, and high alpha values (e.g., Galloway & Cumming 2006). We inferred $\bar{X} < 0.2$ for all bursts, as expected for helium rich bursts. Overall, we matched the observed burst fluences, alphas, and recurrence times to within the 1σ uncertainty of the model.

Based on the agreement between the observed burst properties, we then inferred and modelled composition, base flux, neutron star mass, neutron star radius, distance, and inclination. We set the prior for metallicity to the expected distribution of metallicities based on the location of SAX J1808.3–3658 in the Galaxy, and deduced the most likely CNO mass fraction (metallicity) of the source to be between 0.009–0.019. This range covers the expected value for solar CNO metallicity, which recent work puts at 0.01 (Lodders et al. 2009). We inferred a slightly depleted hydrogen mass fraction of the accreted fuel, of $0.58^{+0.13}_{-0.14}$, indicating that the companion star in this system could be significantly evolved.

We inferred a base flux of 0.25–0.7 MeV/nucleon, which gives an indication of the base heating of the neutron star. We used the constraints on the relationship between NS mass and radius calculated by Steiner et al. (2018) for neutron stars in low mass X-ray binaries in globular clusters as an informed prior for the distribution of acceptable mass and radius combinations and inferred a NS mass between 0.9–1.8 M_{\odot} and a radius between 10.8–13.1 km. The mass is constrained to within 40% (1σ limit) and the radius is constrained to within 11% (1σ limit), indicating that this method cannot constrain neutron star mass and radius to a high precision. This is most likely due to degeneracies in some of the other model parameters, such as base heating (Q_b), that can adjust to produce the same burst energies and recurrence time when the mass, radius, and thus surface gravity and redshift are varied.

Finally, we used the scaling factors we defined and the posterior distributions of the parameters to infer a distance and inclination of SAX J1808.4–3658, based on He & Keek (2016) disc Model A. We found a distance range of 3.1–3.6 kpc for an inclination from the rotation axis of 67° – 73° . Galloway & Cumming (2006) used the fact that the observed bursts showed photospheric radius expansion to infer an upper limit of the distance to the source of 3.6 kpc, just within our 1σ upper limit on the distance. An inclination of 69° , implies both the observed burst and persistent fluxes are artificially increased by reflection from the disc and by the disc itself, bringing the source closer when compared to distance estimates such as Galloway & Cumming (2006) that do not account for inclination.

We have reported the median value and 68th percentile limits of the predicted posterior distributions to give an indication of the parameter values. While this is a representation

of the data, the true solutions are the posterior distributions that were calculated by the MCMC algorithm. Parameters estimated using this technique are limited to the accuracy of the SETTLE model predictions. The benefit of using such a simple model is that it can be used in a MCMC algorithm to effectively sample parameter space.

We have demonstrated that we can infer system parameters of a bursting source using observations of an outburst and the SETTLE model. Future work could apply this method of matching observed properties with models to the other known bursting AMSPs with observations of burst trains, or any accreting neutron star with observations of burst trains. This method enables initial exploration of parameter space, to determine an estimate for the range of parameters for each source. These ranges could then be used in more advanced, computationally expensive models such as KEPLER to narrow down the parameter limits.

ACKNOWLEDGEMENTS

We thank Andrew Casey for his contribution of the metallicity prior we used. We thank Andrew Steiner for helpful discussions regarding the neutron star mass-radius prior. This paper utilizes preliminary analysis results from the Multi-INstrument Burst ARchive (MINBAR), which is supported under the Australian Academy of Science’s Scientific Visits to Europe program, and the Australian Research Council’s Discovery Projects and Future Fellowship funding schemes. AG and ZJ acknowledge support by an Australian Government Research Training (RTP) Scholarship. AH was supported by a grant from Science and Technology Commission of Shanghai Municipality (Grant No. 16DZ2260200) and National Natural Science Foundation of China (Grant No. 11655002). This work benefited from support by the National Science Foundation under Grant No. PHY-1430152 (JINA Center for the Evolution of the Elements). We thank the anonymous referee for constructive and insightful comments that helped to improve the manuscript.

REFERENCES

- Abbott B. P., et al., 2017, *Physical Review Letters*, **119**, 161101
 Abbott B. P., et al., 2018, *Physical Review Letters*, **121**, 161101
 Annala E., Gorda T., Kurkela A., Vuorinen A., 2018, *Physical Review Letters*, **120**, 172703
 Antoniadis J., Tauris T. M., Ozel F., Barr E., Champion D. J., Freire P. C. C., 2016, arXiv e-prints, p. arXiv:1605.01665
 Bildsten L., Chakrabarty D., 2001, *The Astrophysical Journal*, **557**, L29
 Cackett E. M., Altamirano D., Patruno A., Miller J. M., Reynolds M., Linares M., Wijnands R., 2009, *ApJ*, **694**, L21
 Cavecchi Y., Spitkovsky A., 2019, arXiv e-prints, p. arXiv:1905.13735
 Chakrabarty D., Morgan E. H., 1998, *Nature*, **394**, 346
 Cumming A., 2003, *ApJ*, **595**, 1077
 Cumming A., Bildsten L., 2000, *ApJ*, **544**, 453
 Degenaar N., Suleimanov V. F., 2018, arXiv e-prints, p. arXiv:1806.02833
 Elebert P., et al., 2009, *MNRAS*, **395**, 884
 Foreman-Mackey D., Hogg D. W., Lang D., Goodman J., 2013, *PASJ*, **125**, 306
 Fujimoto M. Y., 1988, *ApJ*, **324**, 995

- Fujimoto M., Hanawa T., Miyaji S., 1981, *ApJ*, 247, 267
- Fujimoto M. Y., Sztajno M., Lewin W. H., Van Paradijs J., 1987, *ApJ*, 319, 902
- Galloway D. K., Cumming A., 2006, *ApJ*, 652, 559
- Galloway D. K., Keek L., 2017, arXiv e-prints, p. [arXiv:1712.06227](#)
- Galloway D. K., Cumming A., Kuulkers E., Bildsten L., Chakrabarty D., Rothschild R. E., 2004, *ApJ*, 601, 466
- Galloway D. K., Muno M. P., Hartman J. M., Psaltis D., Chakrabarty D., 2008, *ApJS*, 179, 360
- Galloway D. K., Goodwin A. J., Keek L., 2017, *Publ. Astron. Soc. Australia*, 34, e019
- Gelman A., Roberts G., Gilks W., 1996, Oxford University Press, 16, 17
- Goodman J., Weare J., 2010, *Communications in Applied Mathematics and Computational Science*, Vol. 5, No. 1, p. 65-80, 2010, 5, 65
- Goodwin A. J., Galloway D. K., Heger A., 2018, preprint, ([arXiv:1808.02225](#))
- He C.-C., Keek L., 2016, *ApJ*, 819, 47
- Heinke C. O., Jonker P. G., Wijnands R., Deloye C. J., Taam R. E., 2009, *ApJ*, 691, 1035
- Homer L., Charles P., Chakrabarty D., Van Zyl L., 2001, *Monthly Notices of the Royal Astronomical Society*, 325, 1471
- Johnston Z., Heger A., Galloway D. K., 2018, *MNRAS*, 477, 2112
- Kiziltan B., Kottas A., De Yoreo M., Thorsett S. E., 2013, *ApJ*, 778, 66
- Lewin W. H., Van Paradijs J., Taam R. E., 1993, *Space Science Reviews*, 62, 223
- Lodders K., Palme H., Gail H.-P., 2009, *Landolt Börnstein*, p. 712
- Miller M. C., Chirenti C., Lamb F. K., 2019, arXiv e-prints, p. [arXiv:1904.08907](#)
- Morsink S. M., Leahy D. A., 2011, *ApJ*, 726, 56
- Özel F., Freire P., 2016, *ARA&A*, 54, 401
- Patruno A., Watts A. L., 2012, arXiv e-prints, Psaltis D., Chakrabarty D., 1999, *ApJ*, 521, 332
- Radice D., Perego A., Zappa F., Bernuzzi S., 2018, *ApJ*, 852, L29
- Sharma S., Bland-Hawthorn J., Johnston K. V., Binney J., 2011, *ApJ*, 730, 3
- Steiner A. W., Heinke C. O., Bogdanov S., Li C. K., Ho W. C. G., Bahramian A., Han S., 2018, *MNRAS*, 476, 421
- Strohmayer T., Bildsten L., 2006, *New views of thermonuclear bursts*. pp 113–156
- Taam R. E., 1980, *ApJ*, 241, 358
- Wang Z., et al., 2001, *ApJ*, 563, L61
- Wang Z., Breton R. P., Heinke C. O., Deloye C. J., Zhong J., 2013, *ApJ*, 765, 151
- Wijnands R., 2004, *Nuclear Physics B Proceedings Supplements*, 132, 496
- Wijnands R., van der Klis M., 1998, *Nature*, 394, 344
- Woosley S., et al., 2004, *ApJS*, 151, 75
- Yu H., Weinberg N. N., 2018, *ApJ*, 863, 53
- van Paradijs J., Penninx W., Lewin W. H. G., 1988, *MNRAS*, 233, 437

Table A1. SAX J1808.4–3658 derived neutron star parameters for a fixed mass and radius

Parameter	Value
X	$0.57^{+0.13}_{-0.15}$
Z	$0.012^{+0.004}_{-0.003}$
Q_b (MeV/nucleon)	$0.6^{+0.1}_{-0.1}$
M (M_\odot)	1.4
R (km)	11.2
\dot{m}_{\max} (\dot{m}_{Edd})	$0.035^{+0.002}_{-0.001}$
g (10^{14} cm s $^{-2}$)	1.86
$1+z$	1.26
d (kpc)	$2.9^{+0.1}_{-0.1}$
ξ_b	$0.9^{+0.1}_{-0.1}$
ξ_p	$1.04^{+0.05}_{-0.04}$
$\cos i$	$0.35^{+0.08}_{-0.05}$

APPENDIX A: ADDITIONAL MODEL RUNS

In this section we provide the results of additional model runs carried out in order to robustly test the MCMC code, as well as to replicate past works.

A1 Fixed mass and radius

We held mass and radius constant at $M = 1.4 M_\odot$ and $R = 11.2$ km to replicate the analysis of [Galloway & Cumming \(2006\)](#). The parameter predictions are presented in [Table A1](#) and the probability contours for X , Z , Q_b , d , ξ_p and ξ_b are presented in [Figure A1](#).

The predicted hydrogen mass fraction in [Table A1](#) matches within uncertainty of those predicted by [Galloway & Cumming \(2006\)](#) ($X_0 = 0.54$ for $Z = 0.02$, or $X_0 = 0.5$ for $Z = 0.016$). [Galloway & Cumming \(2006\)](#) inferred a base flux of $Q_b = 0.325$ and a distance of 3.1–3.8 kpc which is just outside the lower limit of our 1- σ range of predictions for these parameters. [Galloway & Cumming \(2006\)](#) used a chi-squared minimisation approach to determine the parameters of interest given a fixed grid of parameters in X , Z and Q_b space to find the best fit burst fluence, recurrence times and alpha values. We used a more robust approach to determine the parameters of interest, and vary more parameters than just X , Z , and Q_b and so we do not expect our results to match exactly with those of [Galloway & Cumming \(2006\)](#). The composition constraints and distance estimate broadly agree with those found by [Galloway & Cumming \(2006\)](#) for a fixed NS mass and radius.

A2 Flat priors on mass and radius

Here we show the parameter limits when assuming a flat prior for mass and radius, rather than the [Steiner et al. \(2018\)](#) probability distribution. The parameter limits are reported in [Table A2](#) and posterior distributions are plotted in [Figure A2](#).

When assuming a flat prior range in mass and radius

Table A2. SAX J1808.4–3658 derived neutron star parameters

Parameter	Value
X	$0.58^{+0.13}_{-0.15}$
Z	$0.013^{+0.006}_{-0.004}$
Q_b (MeV/nucleon)	$0.4^{+0.2}_{-0.2}$
M (M_\odot)	$1.6^{+0.5}_{-0.3}$
R (km)	$11.9^{+1.4}_{-1.2}$
\dot{m}_{\max} (\dot{m}_{Edd})	$0.037^{+0.002}_{-0.002}$
g (10^{14} cm s $^{-2}$)	$1.95^{+0.6}_{-0.4}$
$1+z$	$1.29^{+0.1}_{-0.06}$
d (kpc)	$3.3^{+0.2}_{-0.2}$
ξ_b	$0.74^{+0.1}_{-0.10}$
ξ_p	$0.87^{+0.1}_{-0.10}$
$\cos i$	$0.37^{+0.07}_{-0.05}$

compared to assuming a more informative prior, we find that the mass is equally well constrained in both cases but that the radius is better constrained for the more informative prior run. Otherwise, all parameters remain approximately the same, except for surface gravity, with a stronger surface gravity required by the flat prior run.

This paper has been typeset from a $\text{\TeX}/\text{\LaTeX}$ file prepared by the author.

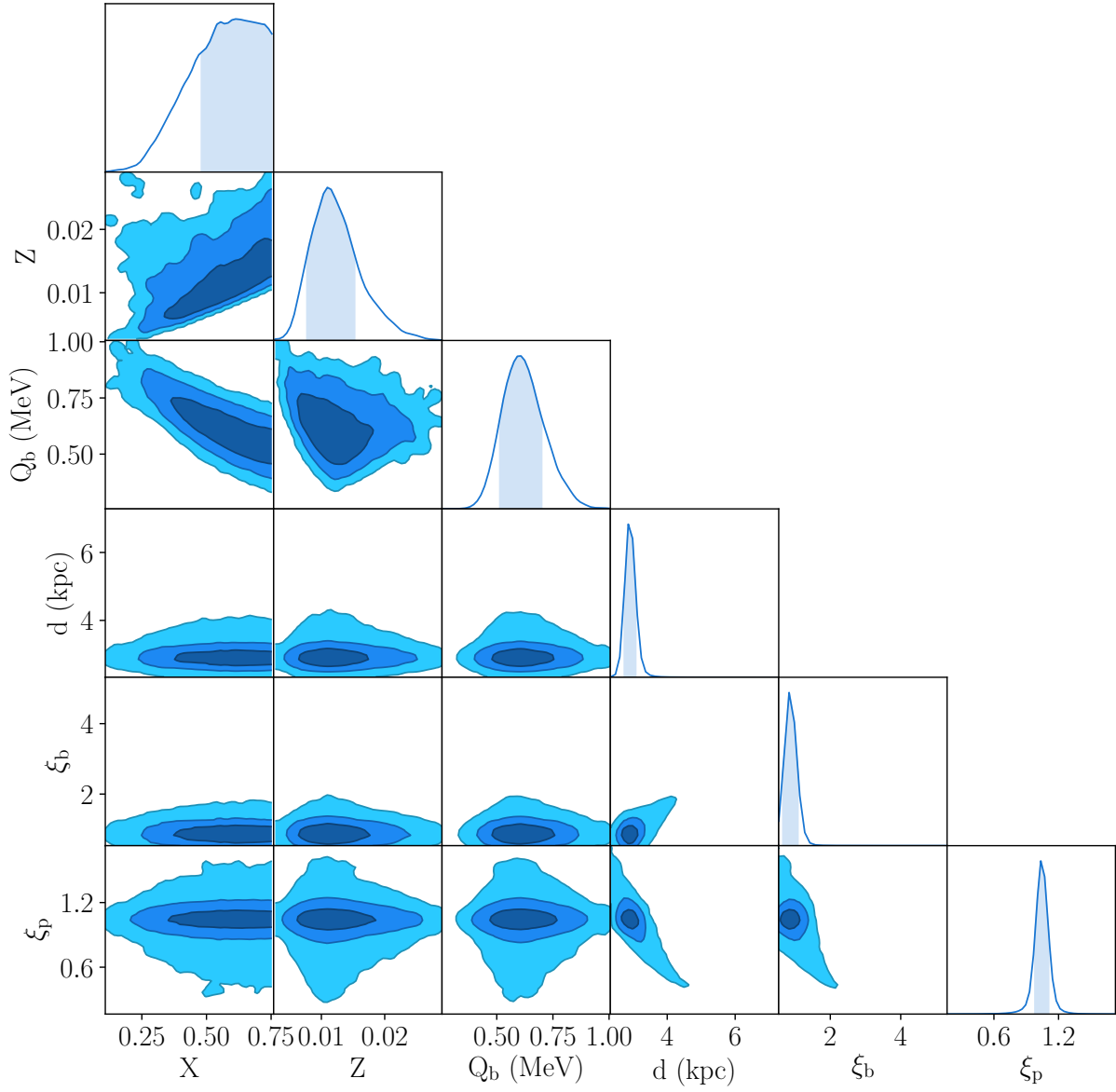


Figure A1. Marginalised probability distributions for hydrogen fraction X , CNO metallicity Z , base flux Q_b , distance d and anisotropy factors ξ_p and ξ_b for the MCMC run with fixed NS mass of $1.4M_\odot$ and radius of 11.2 km .

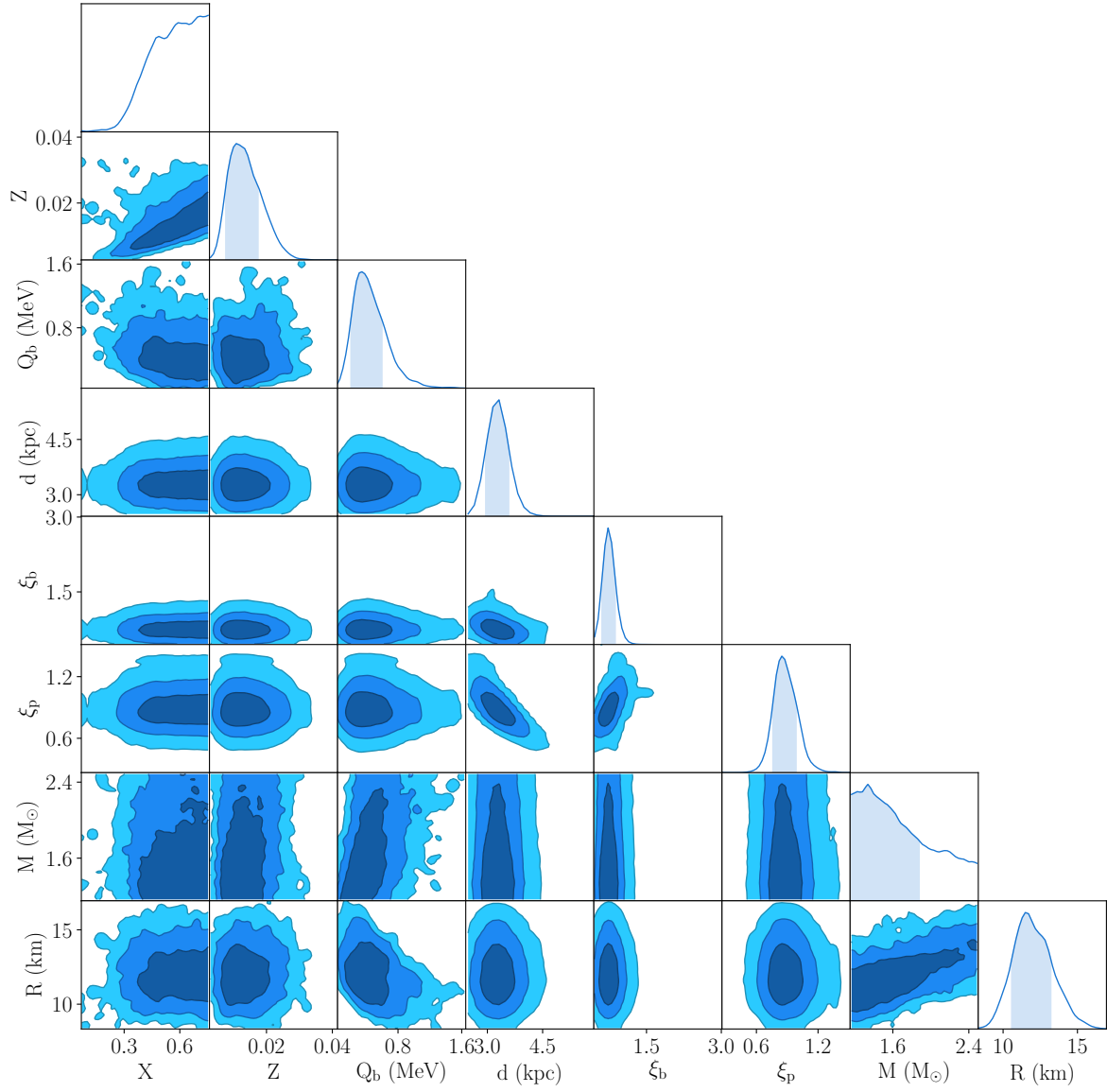


Figure A2. Marginalised probability distributions for hydrogen fraction X , CNO metallicity Z , base flux Q_b , distance d and anisotropy factors ξ_p and ξ_b , NS mass M , and NS radius R for the MCMC run with flat prior ranges for M and R .